Nanoscale Research Letters

RESEARCH

Open Access

Robust Resistive Switching Constancy and Quantum Conductance in High-*k* Dielectric-Based Memristor for Neuromorphic Engineering

Muhammad Ismail[1], Chandreswar Mahata[1], Myounggon Kang[2*] and Sungjun Kim[1*]

Abstract

For neuromorphic computing and high-density data storage memory, memristive devices have recently gained a lot of interest. So far, memristive devices have suffered from switching parameter instability, such as distortions in resistance values of low- and high-resistance states (LRSs and HRSs), dispersion in working voltage (set and reset voltages), and a small ratio of high and low resistance, among other issues. In this context, interface engineering is a critical technique for addressing the variation issues that obstruct the use of memristive devices. Herein, we engineered a high band gap, low Gibbs free energy Al_2O_3 interlayer between the HfO_2 switching layer and the tantalum oxy-nitride electrode (TaN) bottom electrode to operate as an oxygen reservoir, increasing the resistance ratio between HRS and LRS and enabling multilayer data storage. The Pt/HfO_2/Al_2O_3/TaN memristive device demonstrates analog bipolar resistive switching behavior with a potential ratio of HRS and LRS of $> 10^5$ and the ability to store multi-level data with consistent retention and uniformity. On set and reset voltages, statistical analysis is used; the mean values (μ) of set and reset voltages are determined to be -2.7 V and $+1.9$ V, respectively. There is a repeatable durability over DC 1000 cycles, 10^5 AC cycles, and a retention time of 10^4 s at room temperature. Quantum conductance was obtained by increasing the reset voltage with step of 0.005 V with delay time of 0.1 s. Memristive device has also displayed synaptic properties like as potentiation/depression and paired-pulse facilitation (PPF). Results show that engineering of interlayer is an effective approach to improve the uniformity, ratio of high and low resistance, and multiple conductance quantization states and paves the way for research into neuromorphic synapses.

Keywords: Quantum conductance, Neuromorphic synapses, High switching stability, High ON/OFF ratio, HfO_2 switching layer, Interface engineering

Introduction

Because of their simple structure, high-density integration, low power consumption, and fast operation, memristor devices are gaining a lot of interest for memory, logic, neural networks, and sensing applications [1, 2]. In particular, two-terminal device may modify its resistance in response to electrical stimulation of voltage pulses and stores data [3]. Furthermore, memristive devices offer internal computing capabilities and enable a novel computing paradigm, allowing calculation results to be generated and stored on-site without the need for data movement operations, avoiding von Neumann's bottleneck [4]. In oxide-based memristive devices, resistive switching is attributed to the formation/rupture of oxygen-related defects/vacancies or cation migration made conducting filaments [5–7]. Further to explain the

*Correspondence: mgkang@ut.ac.kr; sungjun@dongguk.edu

[1] Division of Electronics and Electrical Engineering, Dongguk University, Seoul 04620, Republic of Korea
[2] Department of Electronics Engineering, Korea National University of Transportation, Chungju-si 27469, Republic of Korea

working principle of the memristive device with an active electrode, electrochemical reaction and cation migration are the most recognized mechanism, which is similar to the valance change mechanism [8]. However, memristive devices based on transition metal oxides, such as HfO_2, Al_2O_3, Ta_2O_5, and ZrO_2 along with others, suffer from non-uniformity in resistive switching parameters, such as instability in resistance values of low- and high-resistance states (LRSs and HRSs), and dispersion in set and reset voltages, which obstruct their commercial applications [9–19]. To address these issues, inserting an interlayer [20, 21], which can function as an oxygen reservoir and possibly controls oxygen ions concentration in the original and inserted layers, thereby improving resistive switching parameters [22], is conducive in enhancing resistive switching performance. In transition metal oxides-based memristive devices, oxygen ions movement and their distribution usually play a substantial role in resistive switching behavior, which is now widely accepted [23, 24]. In a previous work, we have shown that by inserting a thin layer (such as ZTO, CeO_2, TiO_2, and HfO_2) to remove resistive switching parameters instability and their dispersion is a practical and effective method [20, 21, 25–27].

It is worth noting that, in recent years, resistance switching devices are being utilized in advanced brain-inspired applications [28, 29]. Such devices are used to replicate biological processes and so might be the game changer in breaking the von Neumann structural bottleneck. Electrical impulses are able to modify the current flowing through such resistive changing devices; this behavior is analogous to the functions of biological synapses [30–33]. Since in both pre- and post-neurons, a biological synapse changes its weight (equivalent to the conductance of a memristor) by discharging Ca^{2+} or Na^{+} ions [34, 35]. The potentiation and depression are important mechanisms in a biological nervous system, which indicates a deep-rooted transformation in the connection strengths between neurons. According to the interval between presynaptic and postsynaptic action potentials or spikes, the phenomenon of synaptic weight modification is known as spike-timing-dependent plasticity [36]. Due to scalability, low power operation, nonvolatile features, and small on-chip area, memristors are good candidates for artificial synaptic devices to mimic potentiation, depression, and spike-timing-dependent plasticity behaviors [3, 37, 38]. The conductivity of resistive switching devices might be gradually modified by adjusting the input stimuli, like the resistive switching process, in view of ionic migration and charge carrier trapping/detrapping. [39–41] The resistive switching devices could be used to simulate the functions of artificial synapses because their features are identical to those of biological synapses. The nanoscale kinetics for the conduction channel development could explain the progressive shift in conduction under the influence of an electric field [6]. Despite such limitations, the development of conductive routes and their dynamic visualization of neuromorphic behavior have still remained the fundamental and unsolved puzzle that necessitates a significant technological advancement.

Furthermore, reducing the conductive filaments to the atomic scale of quantum point contact permits memristive ballistic electron transport in analog domains without scattering and quantized conductance characteristics [42–44]. It not only dramatically enhances the data storage capability of gadgets, but it also allows neuromorphic systems to analyze information more efficiently. Multiple conductance states of memristor devices should, in general, be realized in as simple a manner as possible for practical use [45–47]. Nonetheless, the most investigations to-date have relied on sophisticated programming approaches to obtain multi-conductance characteristics, with the addition of varying current compliances and voltages putting a strain on the overall circuit design [30, 48, 49]. In resistive switching memristors, improvements are desperately needed not only to simplify the operational philosophy but also to provide dependable and analog-type conductance quantization behavior.

In this paper, we have fabricated $Pt/HfO_2/Al_2O_3/TaN$ bilayer structure through atomic laser deposition (ALD) to explore the multilevel conductance quantization for neuromorphic synapses. Uniform resistance distributions, large ON/OFF ratio ($>10^5$), low working voltage ($-2.9/+1.7$ V), fast speed (1.2/2.0 μs), consistent DC endurance (1000 cycles), AC endurance 10^5 cycles, long-term retention (10^4 s) features, and multilevel quantized conductance states are among the resistive switching characteristics of the memristive device. Interestingly, we have also observed synaptic behavior related to neural learning functions, such as potentiation, depression, and paired-pulse facilitation. The oxygen vacancy-based conducting filamentary schematic model has been proposed to illustrate the resistive switching mechanism. Results show that $Pt/HfO_2/Al_2O_3/TaN$ memristive devices have sufficient potential for their practical applications as high data storage memory and electronic synapses.

Experimental

By creating the structure of $Pt/HfO_2/TaN$ with Al_2O_3 interlayer, two-terminal memristive devices based on HfO_2 film were developed in this experiment. First, a ~ 2 nm Al_2O_3 interlayer was deposited on a TaN/Si substrate through atomic layer deposition (ALD) for 23 cycles utilizing trimethylaluminum (TMA) as the Al source and H_2O as the oxidizing agent (as O_2

source). Then, using ALD, a 5-nm HfO_2 switching layer was deposited using Tetrakis dimethylamino hafnium (TDMAHf) and H_2O as the Hf and O precursors, respectively, with one oxide cycle consisting of 0.5 s Hf metal source injection, 6 s N_2 purging, 0.5 s H_2O injection, and 20 s N_2 purging. At 260 °C, the TEMAH was evaporated. Pure N_2 (99.999 percent purity) was employed as a carrier gas and purge gas. Finally, a 100-nm-thick Pt top electrode with a diameter of 100 µm was deposited with a circular metal shadow mask by using e-beam evaporation technique to obtain the $Pt/HfO_2/Al_2O_3/TaN$ memristive device. Electrical and pulse measurements were taken with a Keithley SCS 4200A parameter analyzer system on a probe station in ambient conditions. Based on the current going from top to bottom electrode, the bias was determined to be positive in this experiment. The cross-sectional view and film thickness of the $HfO_2/Al_2O_3/TaN$ structure were confirmed using a high-resolution transmission electron microscope (HRTEM, JEOL/CEOS, JEM-2100F, Cs corrector). The chemical composition and bonding states of the $HfO_2/Al_2O_3/TaN$ structure were further studied using X-ray photoelectron spectroscopy (XPS, Thermo Fisher K-Alpha) using a monochromatic Al K source ($h\nu = 1486.6$ eV) for photoelectrons excitation. The charge effect was calibrated by setting the C 1s photoemission at 284.6 eV. The XPS depth profile of HfO_2/Al_2O_3 on TaN-coated Si was obtained using Ar ion etching.

Results and discussion

Memristor design and structural characterization

Figure 1 reveals the schematic configuration and structural characterization of $Pt/HfO_2/Al_2O_3/TaN$ memristive device. The schematic construction of a $Pt/HfO_2/Al_2O_3/TaN$ memristive device is shown in Fig. 1a. The HRTEM was used to obtain a cross-sectional view of the HfO_2/Al_2O_3 bilayer film to confirm the thickness of each layer and the formation of an interfacial layer at the Al_2O_3/TaN bottom interface. Figure 1b shows a HRTEM image of the $HfO_2/Al_2O_3/TaN$ structure. HfO_2 and Al_2O_3 films have thicknesses of 5 and 2 nm, respectively. We also did XPS investigations on $HfO_2/Al_2O_3/TaN$ to gain a better understanding of the switching process in the bilayer structure of HfO_2/Al_2O_3 on TaN-coated Si. XPS spectra were fitted with 5% Gaussian–Lorentzian functions after smart-type background subtraction. In the supplementary information, the narrow-scan XPS spectra of Al 2p and Hf 4f are given in Additional file 1: Fig. S1. The Hf 4f peaks of 18.4 eV and 20.05 eV, which correspond to the Hf $4f_{7/2}$ and Hf $4f_{5/2}$ doublets with a 1.65 eV spin–orbit splitting, are consistent with previously published values [50, 51]. Another low-intensity doublet was fitted, corresponding to Hf–O of a non-stoichiometric suboxide bond due to $Hf_x + 4f_{7/2}$ and $Hf_x + 4f_{5/2}$ peaks (× 4) at 17.15 and 18.75 eV, respectively [52]. Two Gaussian–Lorentzian line form peaks are also present in Al 2p spectra. At 75.5 and 74.3 eV, these Al 2p peaks can be found. The

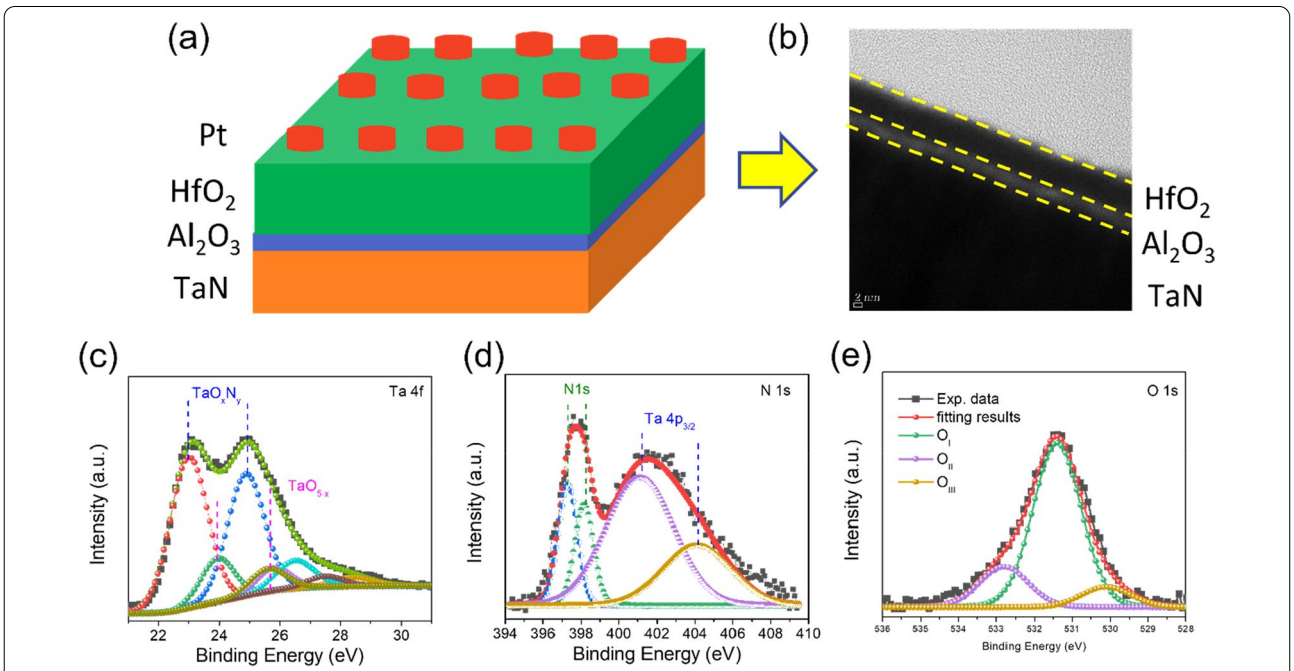

Fig. 1 **a** Schematic diagram of $Pt/HfO_2/Al_2O_3/TaN$ memristive device. **b** Cross-sectional TEM image of $HfO_2/Al_2O_3/TaN$ structure. XPS analyses of TaO_xN_y interfacial layer; **c** Ta 4f, **d** N 1s, **e** O 1s

first peak is attributed to Al–O bonding [53], while the second peak is attributed to Ta–Al–O bonding, which could indicate the decomposition of the Al_2O_3 interlayer, releasing oxygen ions that can react with TaN to form the TaO_xN_y interfacial layer, which is made possible by the oxidization of the TaN electrode during the Al_2O_3 layer deposition [54].

The presence of TaO_x at the Al_2O_3/TaN interface appears to be responsible for the Ta 4f doublet at 24.1 eV and 26.0 eV, as shown in Fig. 1c. At 23.5 eV, another doublet with a lower binding energy and a higher intensity is observed, indicating the production of TaO_xN_y at the Al_2O_3/TaN interface [55]. Multiple peaks in Fig. 1d fit the overlap of N 1 s and Ta $4p_{3/2}$. The TaN electrode has produced two N 1 s peaks at 397.1 eV and 398.1 eV, which represent differing ratios of N bound to Ta [56]. Peaks associated with Ta-N and TaOxNy have generated with binding energies of 401. 2 eV and 404.1 eV, respectively, from core-level Ta $4p_{3/2}$. As a result of these XPS findings, it can be deduced that a thin interfacial layer of TaO_xN_y has developed at the Al_2O_3/TaN contact. This interfacial layer is predicted to play a key role in increasing the memristive device's switching performance. Figure 1e shows the O1s core-level spectrum for the TaO_xN_y interfacial layer. Three separate peaks may be seen in this spectrum. The strong peak at 531.4 eV (O_I) corresponds to oxygen in the TaO_xN_y layer, whereas the higher and lower binding energy peaks at 530.1 eV (O_{II}) and 532.8 eV (O_{III}), respectively, are attributed to hydroxyl and carbonate groups raised from atmospheric exposure due to the TaN metal electrode's high oxygen affinity.

Electrical Characteristics

Figure 2a displays the schematic diagram of Pt/HfO_2/Al_2O_3/TaN memristive device used for the electrical measurements performed by Keithley 4200-SCS parameter analyzer. The TaN electrode is used to define the bias polarity. The I–V characteristics of the Pt/ HfO_2/Al_2O_3/TaN memristive device are shown in Fig. 2b. The high-resistance state (HRS) of the pristine device is the virgin condition, with a resistance of $> 10^{10}$ at 0.2 V read voltage. An electrical forming technique with high voltage is required to induce reproducible resistive switching behavior in the virgin Pt/ HfO_2/Al_2O_3/TaN memristive device. At 5.05 V of applied negative voltage to the Pt electrode with a 5-mA compliance current, memristive

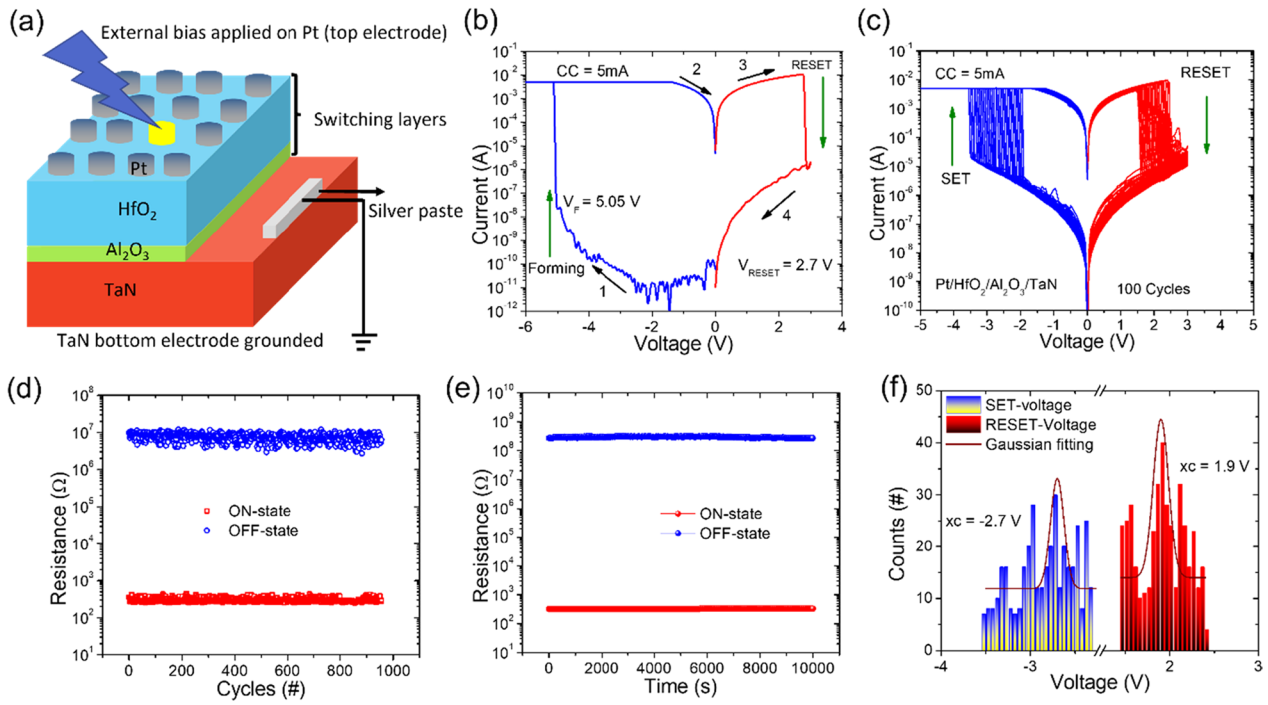

Fig. 2 **a** Schematic diagram of Pt/HfO_2/Al_2O_3/TaN memristive device in electrical measurement configuration, which shows that the external voltage is applied to the Pt top electrode with the TaN bottom electrode electrically grounded. **b** I–V curves of an electroforming process (blue) and reset process (red). The arrows and numbers represent voltage sweep directions and sequences, respectively. **c** Typical bipolar I–V characteristics of 100 consecutive cycles, where green arrows indicate the set and reset directions. **d** DC endurance test results over 1000 cycles; the values of ON-state and OFF-state resistances were read at ± 0.2 V under ambient conditions. **e** Data retention characteristics of ON state and OFF state under a constant voltage stress of 0.2 V for 10^4 s at room temperature. **f** Statistical distribution analyses of set and reset voltages for the 100 switching cycles

device current abruptly increases, suggesting that the memristive device transitions from the initial-resistance state (IRS) to the low-resistance state (LRS), as illustrated in Fig. 2b. The reset process occurs at a positive bias of about + 2.7 V, where the memristive device switches from LRS to HRS. In order to investigate the average electroforming voltage of the memristive devices, electroforming process was performed on twelve randomly selected memristive cells. Additional file 1: Fig. S2(a) shows the box chart of electroforming voltage of twelve memristive cells, which represent the distribution of formation sites in the conductive filaments and are related to the operating voltage of memristive device. Average electroforming voltage was calculated and is to be − 4.95 as shown in Additional file 1: Fig. S2(b). Furthermore, to examine the electrical homogeneity for high-density memory applications, stability and reproducibility during set and reset operations are of utmost importance. Figure 2c shows the typical I–V curves of 100 continuous set and reset cycles on the Pt/HfO_2/Al_2O_3/TaN memristive device. In the set process under negative bias, only a sudden increase in current is noted, while reset transitions in the positive voltage sweep involve either abrupt (single state) or multi-state transformations. These set and reset processes could only be possible for the opposite bias polarities indicating that the memristive device displays the bipolar resistive switching effect.

Furthermore, one of the most significant properties for nonvolatile memory applications is direct current (DC) cycling endurance. The Pt/HfO_2/Al_2O_3/TaN memristive device has such endurance properties, as shown in Fig. 2d. Switching qualities that are steady and repeatable have been established. At room temperature, the sweeping voltage was applied from 0 to 5 V for set and 0 to 3 V for reset, with a reading voltage of 0.2 V. This endurance test illustrates an excellent durability during continuous 1000 switching cycling. The ON/OFF ratio between HRS and LRS remains around 10^5 during direct DC switching operation. The data retention properties of the Pt/HfO_2/Al_2O_3/TaN memristive device were further confirmed by monitoring the time-dependent evolution of resistance values in both the LRS and HRS at room temperature. After applying negative (− 5 V) and positive (+ 3 V) bias voltages for a short time, the ON-state and OFF-state resistances were read out. With a read voltage of 0.2 V, the resistance magnitudes were recorded every 10 s. Both LRS and HRS, as shown in Fig. 2e, were constant for 10^4 s with no discernible decline. After removing the power supply for more than 104 s, the memristive device remains in the ON/OFF state, indicating that it is nonvolatile. The statistical distribution studies of the set and reset voltages of the Pt/HfO_2/Al_2O_3/TaN memristive device are shown in Fig. 1f. Set and reset voltages are found to have typical values of − 2.7 V and 1.9 V, respectively.

The memristive devices performance and memory window could thus be improved by a bilayer or multilayer design. The memristive device with the Pt/HfO_2/Al_2O_3/TaN structure has better time switching stability and reproducibility. As a result, the memristive devices switching stability and consistency were investigated further. Over 120 switching cycles, the dependability and reproducibility of nine randomly selected memristive devices were validated. The typical I–V characteristics of the nine memristive devices are shown in Additional file 1: Fig. S3 (a–i). In addition, as shown in Additional file 1: Fig. S4 (a–i), an endurance test was undertaken. Each memristive device showed consistent switching behavior with no discernible deterioration between the ON and OFF states. The memristive device high ON/OFF resistance ratio (10^5) and switching characteristics make it ideal for use as electronic synapses.

Multilevel Data Storage Capability by Controlling Current Compliance

The literature reports [17, 21, 31] that compliance current is a key factor to influence the resistance distributions during switching operation. During testing operations of memristive devices, a current compliance is usually applied to protect the devices from hard breakdown. In addition, current compliance can greatly affect the conductive filament size in demonstrating the multilevel storage capability [19, 57]. That is why, in the present study, different current compliance magnitudes were applied as varied from 0.5 to 5.0 mA, which are capable to modulate the conductive filament size leading to multilevel data storage capability. Figure 3a–d shows the typical bipolar I–V characteristics of 120 cycles. During measurements, set and reset processes were adjusted with respective voltage sweep of − 5 V and + 3 V under different current compliances (such as 0.5 mA, 1 mA, 3 mA, and 5 mA). Moreover, the reset process was kept free from current compliance. Endurance performance under different current compliances is shown in Fig. 3e–g. Note that current level during ON state under different current compliances (i.e., 0.5 mA, 1 mA, 3 mA, and 5 mA) was almost similar. It means that thicker filaments are formed during set process, so that higher reset voltages are required to rupture thicker conductive filaments. In addition, I–V characteristics were examined by randomly selected memristive cells under varying current compliance (1 mA, 3 mA, and 5 mA) to further corroborate the influence on the ON state of the resistance, as shown in Additional file 1: Fig. S5 (a-e). Only switching cycling uniformity is enhanced by increasing current compliance, almost in the same way as single cell

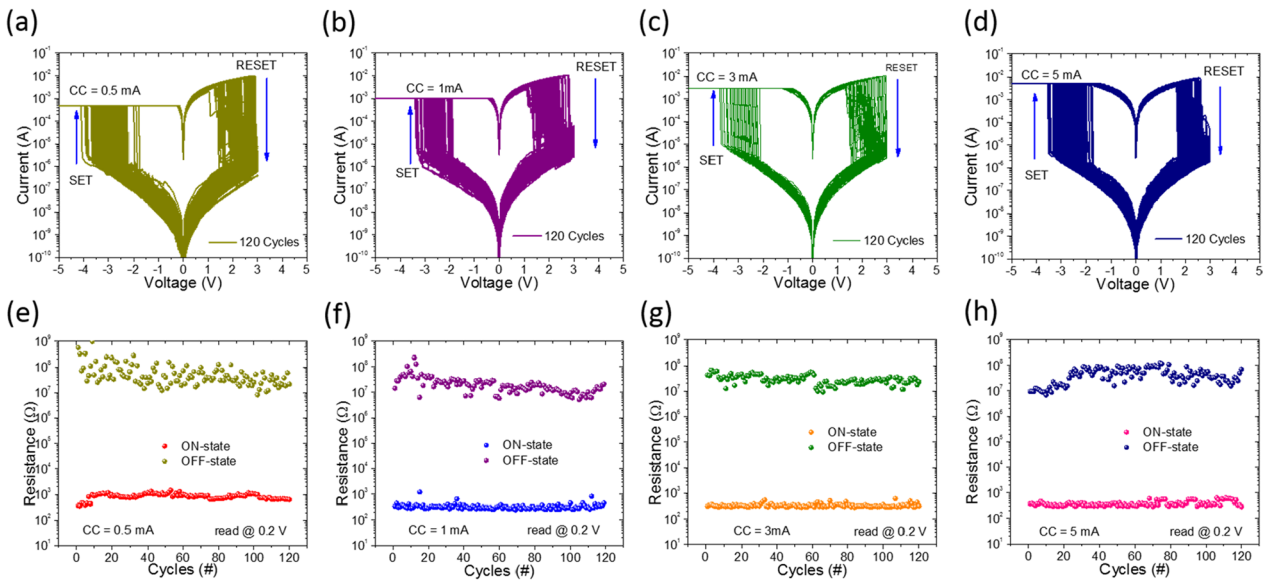

Fig. 3 **a**–**d** Typical bipolar I–V curves, and **e**–**h** endurance performance of Pt/HfO_2/Al_2O_3/TaN memristive devices at different current compliances of 0.5 mA, 1 mA, 3 mA, and 5 mA

memristive properties are improved by raising current compliance. The schematic representation of a switching mechanism with various current compliances is shown in Additional file 1: Fig. S6. The size (diameter) of conductive filaments does not increase even though additional oxygen vacancies are accumulated under different current compliances, according to the filamentary model. We conclude that memristive devices have capability to operate at each current compliance in almost same manner for its nonvolatile memory applications. All these results indicate that current compliance in the present case does not significantly influence the ON/OFF resistance ratio suggesting that the bilayer memory device is locally conductive and obeys the model of conducting filaments.

Multilevel Data Storage Capability by Adjusting $V_{RESET\text{-}stop}$

The I–V curves of Pt/HfO_2/Al_2O_3/TaN memristive device are drawn in Fig. 4a under different stop voltages, i.e., + 2.0 V and + 3.0 V. Monitoring the compliance current at 1 mA during the set process performed under different reset-stop voltages, electrical resistance in the OFF state is noticed to be distinct for the same individual memory cell. Further note that memristive device gradually switched from LRS to HRS under reset-stop voltage of 2.0 V, which reveals its great potential for application in neuromorphic computing, as gradual switching is necessary for neuromorphic synapses. Moreover, as the memristive device abruptly switched from LRS to HRS on increasing reset-stop voltage to 3.0 V, revealing that it can be used for data storage. To test the ON/OFF ratio at different stop voltages, the 100 consecutive switching cycles were performed 100 times. At a read voltage of 0.2 V, the ON and OFF states were retrieved. Figure 4c depicts the HRS and LRS resistance distributions. Note that by increasing the reset voltage beyond 2.0 V, the memristive device dramatically raised the resistance up to 4 orders of magnitude. It means that conductive filaments are completely ruptured at 3.0 V reset-stop voltage, which is responsible for high ON/OFF ratio. It is concluded that the higher-stop voltages in the reset process, the higher resistance values of HRS could be achieved under the same compliance current. The multilevel storage can be explained by the oxygen vacancy filaments with a conical shape formed by the set process which were thinned and ruptured gradually by controlling the reset-stop voltage [58]. Based on conductive filament theory, we have proposed a physical model to explain the enlargement of ON/OFF ratio or the large memory window [21, 26, 27]. Figure 4d, e shows the schematic diagram of different reset-stop voltage (+ 2.0 V and + 3.0 V)-dependent switching mechanisms of Pt/HfO_2/Al_2O_3/TaN memristive device. The magnitude of HRS level depends on the proportion of filament that dissociates under a positive electric field. When the reset-stop point is small (+ 2.0 V), a slight amount of filament in the dielectric layer dissolves and, consequently, resistance change was less. When the higher positive voltage is applied (+ 3.0 V), the maximum HRS level was achieved. Clearly, a larger tunneling gap between the filament tip

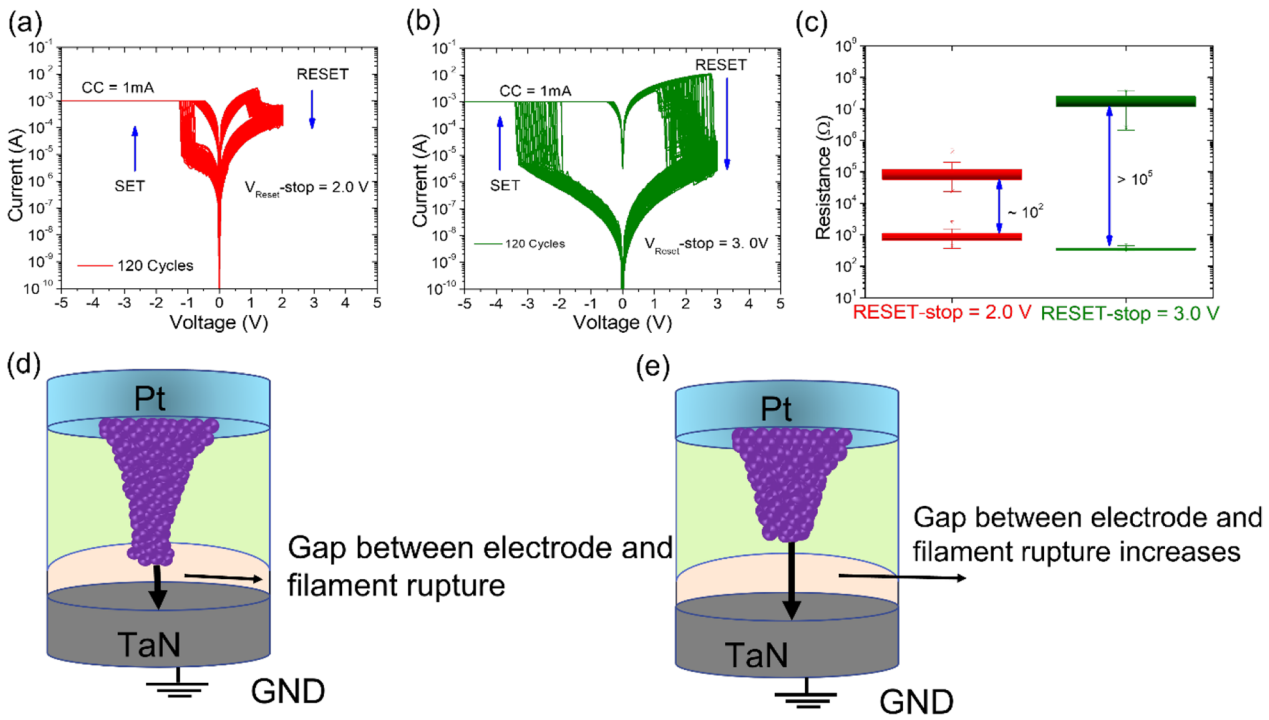

Fig. 4 **a** Typical bipolar I–V characteristics and **b** comparison of ON/OFF resistance ratios of the Pt/HfO_2/Al_2O_3/TaN memristive device under different reset-stop voltages, i.e., + 2.0 V and + 3.0 V, with fixed set voltage of − 5 V. **c**, **d** Schematic illustration of switching mechanism of OFF state at different reset-stop voltages (2.0 V and 3.0 V) for the prepared Pt/HfO_2/Al_2O_3/TaN memristive device

and the electrode increases the Schottky barrier height [59]. Because of the expanding Schottky barrier height, the reset current should decrease as the reset-stop voltage rises. The reset current level approaches a steady plateau with only minor fluctuations as the reset-stop voltage is increased. The space between the tip of the conductive filaments and the electrode, which can vary greatly from cycle to cycle, is smaller at lower reset-stop voltage [60]. Besides, by employing greater reset-stop voltage, all conductive filaments were ruptured, which is responsible for decreasing the OFF-state resistance. It means that rupture of the conductive filament is maximum at reset stop of 3.0 V for maximum enlarging the gap between the ruptured filaments, resulting in a higher resistance state. Results show that Pt/HfO_2/Al_2O_3/TaN memristor device has great potential for application in neuromorphic and long data storage.

Quantized Conductance States

The quantized effect observed during the reset process is demonstrated in Fig. 5a, which exhibits I–V curves for the slow sweep measurement mode (delay time = 0.1 s, step voltage = 0.005 V). During such reset processes, there noticed drops of current magnitudes in several steps. The corresponding conductance–voltage curves for the reset operation are also drawn as shown in Fig. 5b. Again, voltage is increased in 0.005 V increments with a 1 s delay between each step. The $G = I/V$ was used to compute the electrical conductance (G) measured in units of the conductance of a single atomic constant. The quantum of conductance (77.5 μs) is: $G_0 = 2e^2/h$, where e is the charge of an electron and h Planck's constant [61]. When memristive conductance falls below 1 G_0 at + 2.5 V, the atomic/electronic contact is disconnected, and consequently, memristive device switches to its OFF state. Charge tunneling between the filament and the electrode dominates the conductivity of the memristive device in its OFF state. The charge tunneling distance is continuously extended when positive voltage bias is increased, resulting in a continuous rise in resistance in the OFF state. Multiple conductance states observed in the resistive devices are useful in artificial synapse applications, according to these findings [62–65].

Pulse Endurance Characteristics

A pulse mode was initiated to test the switching speed between the ON and the OFF states to further investigate the synaptic characteristics of Pt/HfO_2/Al_2O_3/TaN memristive device. Between the read pulses, we apply either set- or reset-pulse response to demonstrate the short

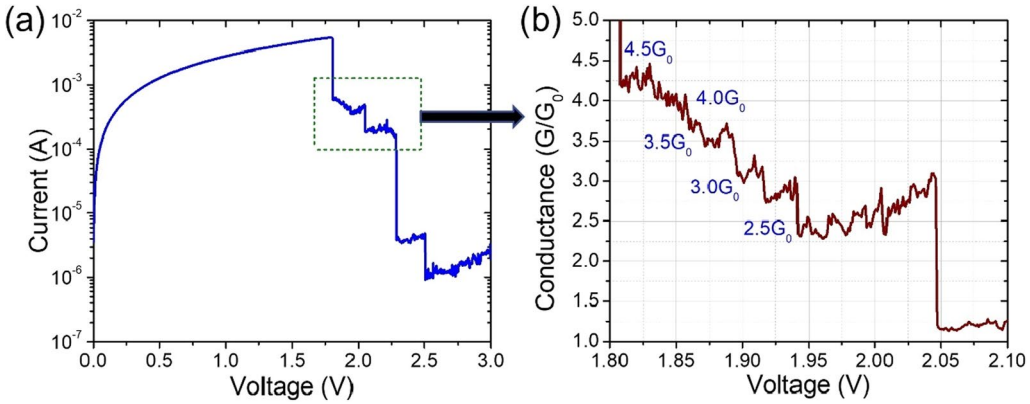

Fig. 5 Noticeable quantized changes in the conductance of Pt/HfO_2/Al_2O_3/TaN memristive device: **a** I–V curves during the reset process for slow DC sweep cycles. **b** Conductance–voltage curves revealing the quantum conductance effect. The voltage is increased in steps of 0.005 V and delay time of 0.1 s per step

current characteristics. With an effective pulse width of 500 µs, the set/reset voltage was—4.0 V/ + 3.5 V. The typical write/erase speeds of the Pt/HfO_2/Al_2O_3/TaN memristive device under read/set and reset/read bias pulses are shown in Fig. 6, where blue line represents the input bias, and red line represents Pt/HfO_2/Al_2O_3/TaN memristive device response current. As illustrated in Fig. 6a, the read operation (at 0.2 V) before applying the set or the reset pulses clarifies the previous (or initial) state of the device resistance, whereas the read operation after

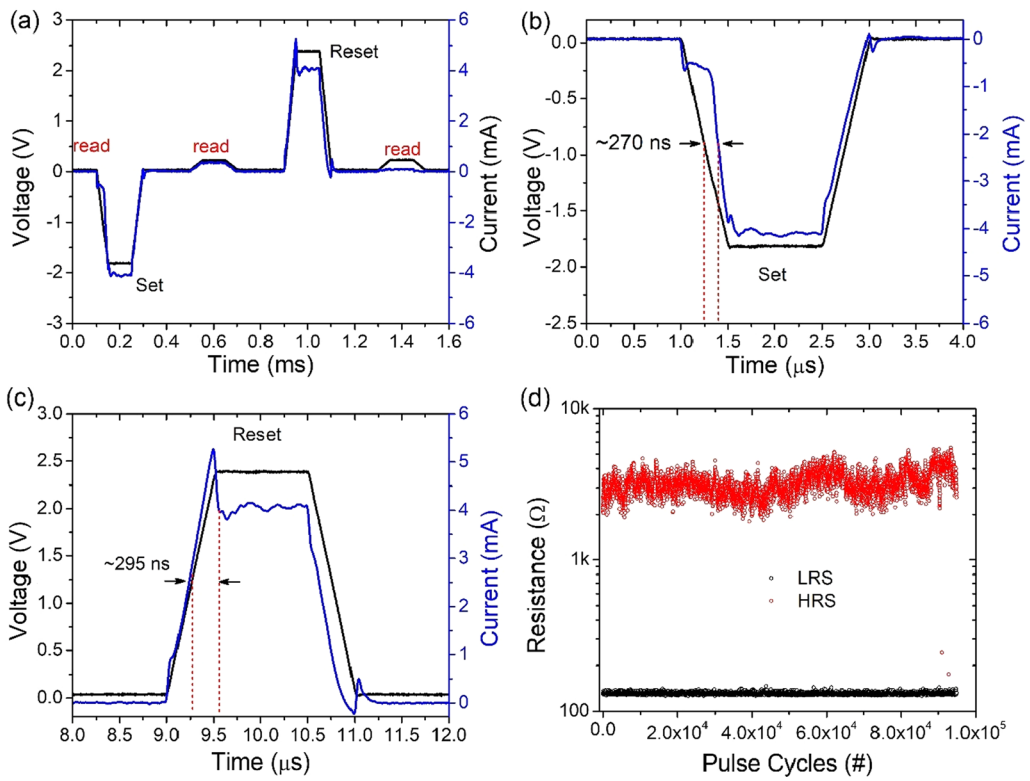

Fig. 6 Pulse response characteristics of the Pt/HfO_2/Al_2O_3/TaN memristive device: **a** current response during set and reset process under negative and positive bias pulses, respectively. **b** Set response time is about 270 nm and **c** Reset response time is about 295 ns, which are represented by red dashed lines. **d** Pulse endurance test. Device switched with 10 × difference in HRS and LRS and suffered no read/write disturbance after more than 10^5 cycles

applying the set/reset pulses proves the correctness of the set/reset operation. The delay time between the response current and the input set or the output reset bias in the middle of leading edge is specified as the set/reset speed (Δt). As a result, under the bias of −2.0 V/+2.5, V with 12 µs pulse width, the set and the reset response time of $Pt/HfO_2/Al_2O_5/Pt$ memristive device is about ~ 270 ns and 295 ns, respectively, as illustrated in Fig. 6b, c. As shown in Fig. 6d, continuous alternating current (AC) pulse operation for up to 10^5 cycles was carried out without failure, proving the high capability for continuous AC operation of this $Pt/HfO_2/Al_2O_3/TaN$ memristive device.

Neuromorphic Characteristics

Multilevel storage is not only a powerful technique to overcome the restrictions of low-density storage, but it also serves as a link between memory and neuromorphic computing. According to the literature, memristive device multilayer conductance capability is an additional property that is beneficial for artificial synapse applications [66–69]. Such multilayer I–V characteristics are shown in Fig. 7a for different reset-stop voltages ranging from 0.7 V to 1.0 V. The 0.01 V was the step increase during this operation. Because of such low increment in the stopping voltage, fifteen conductance states were obtained that correspond to partial rupturing of oxygen vacancies-based conductive filaments [70]. Multilevel retention tests were also carried out by varying the reset-stop voltage (0.7 V to 2.0 V), as shown in Fig. 7b. During continuous stress of 0.2 V for 500 s, retention tests of fifteen different states were performed, which verify the nonvolatile behavior and indicate that the memristive device is suitable for multi-level data storage memory. Additionally, potentiation and depression tests were performed for 50 consecutive cycles to imitate the synaptic function of the memristive device, as illustrated in Fig. 7c. Conductance of the memristive device can effectively be potentiated (conductance gradually increases)

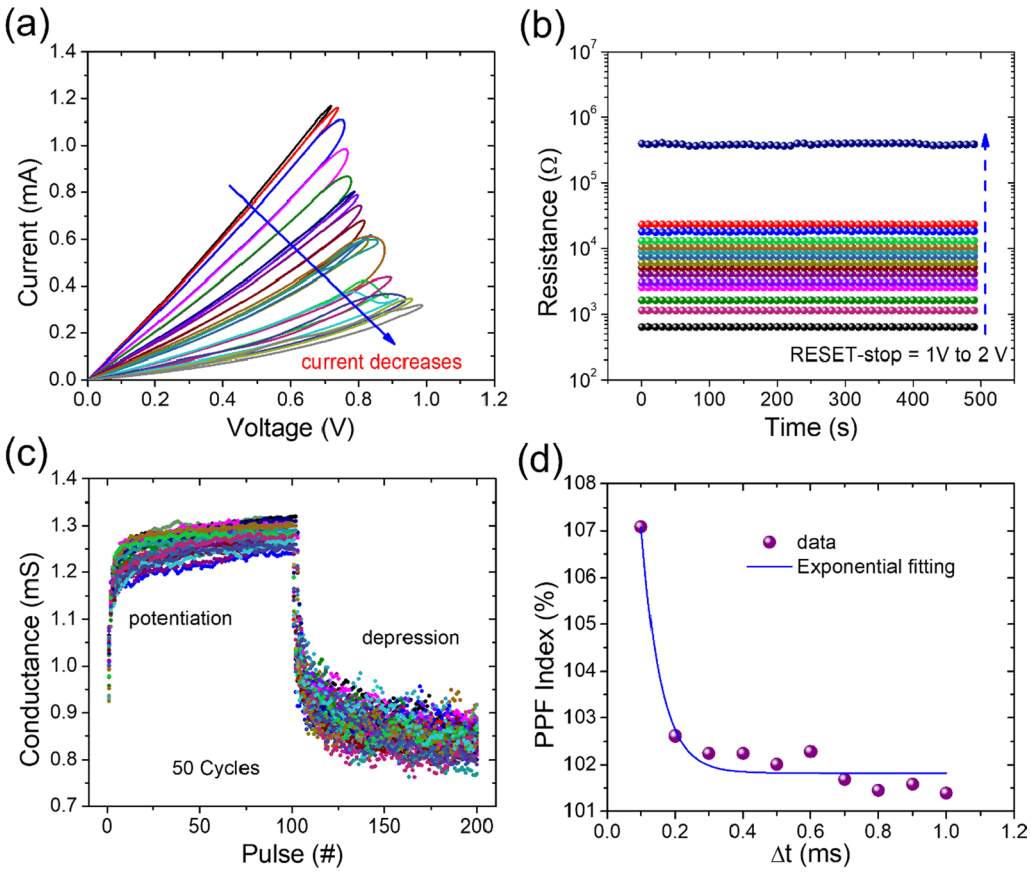

Fig. 7 **a** Multilevel conductance states during reset process by applying a consecutive increase in reset voltage sweep from 0.7 to 1.0 V. Arrow indicates the sweep direction. The increment of sweep voltage was 0.01 V. **b** Retention tests were performed at fifteen different HRSs for 500 s. The resistance values were extracted at read voltage of 0.2 V. **c** The potentiation and depression characteristics under 50 negative pulses (− 1.0 V, 500 µs) and 50 positive pulses (+ 1.5 V, 500 µs), respectively. **d** The PPF index vs. pulse interval Δt, where a series of double spikes with different inter-spike timings were employed, showing an exponential decreasing trend

and depressed (conductance gradually lowers) using fifty negative pulses and fifty positive pulses, respectively. To activate the potentiation and depression features in the resistive device, the pulse amplitude was tuned to −1.0 V/+1.5 V, while the pulse width to 500 s. Notice that after 40 cycles of potentiation and depression, the memristive device remained intact leading to its strong stability and repeatability so that it can be utilized to build artificial synapses in neuromorphic computing systems. The PPF (paired-pulse facilitation) is a physiological phenomenon linked to short-term plasticity in which a previous stimulus enhances a synaptic response to a future stimulus [71]. The interval between the two pulses was altered from very short to extremely long to assess the memristive device's PPF behavior over a wide variety of pulse intervals. Figure 7d illustrates such measured PPF behavior of the memristive device at various pulse intervals. As analogy with biological synapses, PPF index drops as the pulse interval increases [72]. Calculating a PPF index from the expression (I_2/I_1), where I_1 and I_2 are the peak amplitudes of the first and second responses, respectively, can be used to estimate changes in the PPF [73]. The PPF index for double pulse stimulation with the smallest pulse interval was the highest (i.e., 107). The dual stimuli with a longer gap, on the other hand, had the lowest PPF index of 102. PPF behavior was absent or inadequate in double stimulations with much longer pulse intervals. The PPF index in biological synapses is generally dependent on the interval between paired presynaptic stimulations, which our memristive device successfully simulates.

Resistive Switching Mechanism

We propose a model to provide comprehensive insight into the RS mechanism of the pristine state, set state, and reset state of the Pt/HfO_2/Al_2O_3/TaN memristive device, based on the above-mentioned electrical and other material characteristics research, as shown in Fig. 8. The memristive device switching behavior and performance are determined by the work function (ϕ) difference between the electrodes (top and bottom), as well as the electron affinity (χ) difference between the switching layers (HfO_2 and Al_2O_3). TaN has a value of work function (ϕ) 3.4 eV, which is lower than Pt (5.65 eV). [74] The χ values of HfO_2 and Al_2O_3 are 2.85 eV and 0.9 eV, respectively [75, 76]. E_v and E_c represent the valence and conduction band edges of HfO_2, respectively, while E_g represents the band gaps, which are 5.8 eV (HfO_2) and 8.0 eV (Al_2O_3). The Al_2O_3 has much lower value of χ but possesses higher band gap value than that of HfO_2, allowing electrons to move from Al_2O_3 to HfO_2 layer (possessing higher electron affinity), resulting in larger electron concentration in the dielectric matrix. The differences between the values of ϕ and χ are responsible to create a barrier height. As a result, the junction produced by the TaN bottom electrode and the Al_2O_3 interlayer has a substantial Schottky barrier of around 3.71 eV, which is higher than the 3.09 eV for the interface formed by the

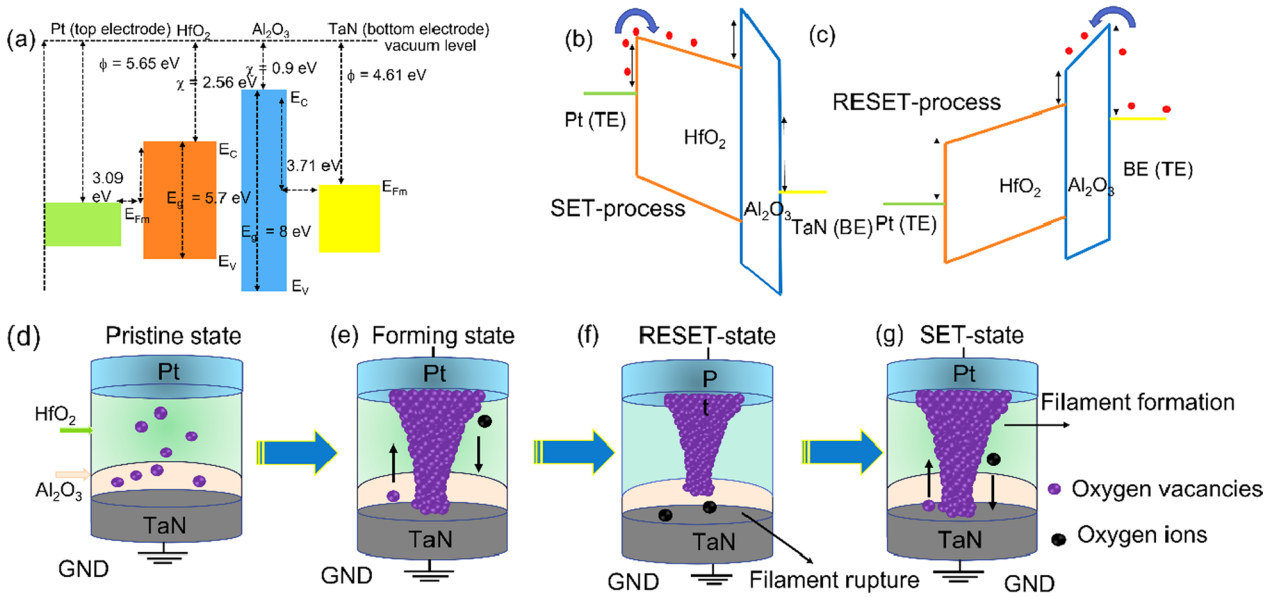

Fig. 8 Relative energy band diagrams and conduction model: **a** before applying electric field (zero bias), **b** ON state (forward bias), and **c** OFF state (reverse bias) of Pt/HfO_2/Al_2O_3/TaN memristive device. Physical model of resistive switching behaviors: **d** pristine state, **e** set process (conductive filaments creation under negative bias), and **f** reset process (filament ruptured under positive bias) of the Pt/HfO_2/Al_2O_3/TaN memristive devices

Pt top electrode and the HfO_2 layer, as shown in Fig. 8. An asymmetric Schottky barrier is projected to emerge at the top HfO_2/Pt contact due to the energy difference. Analog bipolar switching is caused by a work function mismatch of 2.25 eV between the inert Pt top electrode (5.65 eV) and the high oxygen affinity TaN bottom electrode (3.4 eV) [77]. Figure 8a shows the steady-state conduction band diagram at zero bias. When a negative voltage bias is supplied to the top Pt electrode, Schottky barrier Al_2O_3/TaN bottom interface regulates electron drift toward TaN bottom electrode at a negative voltage, as illustrated in Fig. 8b. Oxygen ions transport toward the Al_2O_3 layer and hence to the TaN bottom electrode from the upper HfO_2 layer. Oxygen ions return to the Al_2O_3 and HfO_2 layer when a positive bias is supplied to the Pt top electrode. As shown in Fig. 8c, the Schottky barrier at the Pt/HfO_2 interface limits electron injection at positive voltage and is limited by the discontinuity of the conduction band at the Al_2O_3/HfO_2 contact. Based on the XPS results (see Fig. 1), a potential switching mechanism for the Pt/Al_2O_3/HfO_2/TaN memristive is presented, which considers the TaN electrode chemical activity with oxygen and the non-distribution of oxygen vacancy concentration in the HfO_2/Al_2O_3 dialectics.

Finally, a conducting model is proposed to explain the resistance switching mechanism based on the results of electrical measurements. The role of TaO_xN_y in the reset and set process is the key to understanding this proposed combined model. Previously reported that TaN electrode act as a reservoir for oxygen ions drifting under the applied voltage [10]. Because the Gibbs free energies of the interfacial TaO_xN_y layer (− 604.0 kJ/mole) is higher as compared to Al_2O_3 layer (-1076.0 kJ/mole) and as well as upper HfO_2 layer (− 1010.8 kJ/mole).[78, 79]. The set and reset occurs at TaO_xN_y interface which also acts as the switching region. Figure 8d displays the pristine state of the memristor device. When a negative voltage is applied on the Pt top electrode caused oxygen ions to drift from the insulating layer to the high oxygen affinity TaN bottom electrode, leading to the formation of TaO_xN_y interfacial layer. The memristive device switches from OFF state to ON state (forming), as shown in Fig. 8e. When a reverse reset voltage is applied to the memristive device, the bottom electrode TaO_xN_y acts as an oxygen reservoir. The oxygen ions migrate back to the high-k oxide layer and fill the oxygen vacancies. Then, a gap forms in the insulating layer and consequently the tip of conductive filaments is allowing to reset back from ON to OFF state, as shown in Fig. 8f. Moreover, the insulating gap helps to enhance the electric field between the filament and metal electrode, and therefore, oxygen ions in the insulating layer can overcome the barrier from the metal [80]. These oxygen ions can recombine with the vacancy to form the insulating oxide at the filament tip. Therefore, the resistance increases (Fig. 4). Again, by applying negative bias to the top electrode, oxygen ions migrate from high-k insulating layer to TaO_xN_y interfacial layer, forming conductive filaments again between the two electrodes and switching the device from OFF to ON state (Fig. 8g). In this switching model, it is easy to explain that the bipolar switching phenomena can easily occur in Pt/HfO_2/Al_2O_3/TaN structure with a non-symmetrical electrode configuration. Besides as an oxygen reservoir, the TaO_xN_y interfacial layer also functioned as oxygen ion barrier [81, 82] from the resistive switching function layers, which may be responsible for improved switching endurance property, tight distribution in set/reset voltages, extended duration stability, and large memory window of Pt/HfO_2/Al_2O_3/TaN structure.

Results of performance comparison between current work and previously reported HfO_2-based bilayer and trilayer memristors are summarized in Table 1.

Table 1 Performance comparison of HfO_2-based bilayer and trilayer memristor

Memristor structure	Forming voltage (V)	Operating voltage (V)	ON/OFF ratio	Endurance (cycles)	Retention (s)	Switching polarity	Switching mechanism	References
Pt/HfO_2/Al_2O_3/TaN	− 5.06	− 2.7/+ 1.9	~ 10^5	1000	10^4 s	Bipolar	ECM	This work
Ti/TiO_2/HfO_2/Si	Free	+ 10/− 6.0	~ 10^2	~	10^4 s	Bipolar	VCM	[83]
Al/AlO_x/HfO_x/Pt	~	+ 1/− 2.0	~ 103	~ 400	10^4 s	Bipolar	VCM	[84]
Pt/HfO_2/SiO_2/TaN	− 5.0	− 1.9/+ 2.7	~ 10^4	1000	10^4 s	Bipolar	ECM	[52]
Pt/Al_2O_3/HfO_2/HAlfO$_x$/TiN	Free	− 1.0/+ 1.2	~ 10^2	1000	10^4 s	Bipolar	ECM	[11]
TaN/HfO_2/Al2O_3/HfO_2/ITO	–8.2	− 0.8/+ 1.0	~ 10	1000	10^4 s	Bipolar	VCM	[85]

Compared to other bilayer and trilayer memristors, HfO_2-based bilayer resistive switching memristor demonstrated noticeable advantages such as lower operating voltages, high endurance, and large ON/OFF ratio ($>10^5$). These comparative analyses signify that bilayer HfO_2-based memristor is potential candidates for nonvolatile memory and neuromorphic systems.

Conclusions

By inserting the high band gap and low Gibbs free energy thin Al_2O_3 interlayer, high resistive switching stability, neuromorphic synapses, and quantum conductance were demonstrated in the $Pt/HfO_2/Al_2O_3/TaN$ memristive device. HRTEM study confirms the structure and thicknesses of the high-k dielectric HfO_2 and Al_2O_3 films. A small layer of TaO_xN_y occurs at the Al_2O_3/TaN contact because of Ta strong oxygen accumulation characteristic, as shown by XPS analysis. The $Pt/HfO_2/Al_2O_3/TaN$ memristive device demonstrates stable analog bipolar resistive switching behavior with five orders of ON/OFF resistance ratio, according to the results. For retention and endurance tests, the above-indicated ON/OFF resistances ratio in the LRS and HRS was maintained after continuous 1000 DC switching cycles, 10^5 AC switching cycles, and nonstop ± 0.2 V stress up to 10^4 s. Quantum conductance was also found in the reset process when the DC voltage sweep rate was reduced. Furthermore, for high-density storage, multilayer conductance states were controlled by interrupting reset voltage. During the set and reset processes, the switching speed was to be 270 ns and 295 ns, respectively. Finally, biological synaptic actions like long-term potentiation (increases), long-term depression (decreases), and paired-pulse facilitation timing are all rigorously proven. This research demonstrates that using high band gap and Gibbs free energy thin layer of Al_2O_3 as an interlayer can improve ON/OFF ratio, uniformity, stability, and reproducibility. The memristive device also has significant promise in multilevel quantum conductance and artificial synapses applications, although current memristive device still has disadvantages such as high-power consumption, abrupt set/reset switching, and electroforming process. In future work, we will try to overcome these issues by interface engineering of the memristive devices.

Abbreviations

LRSs and HRSs: Low- and high-resistance states; PPF: Paired-pulse facilitation; ALD: Atomic laser deposition; TMA: Trimethylaluminum; TDMAHF: Tetrakis dimethylamino hafnium; HRTEM: High-resolution transmission electron microscope; XPS: X-ray photoelectron "HRS and LRS of $>10^5$" spectroscopy; IRS: Initial resistance state; DC: Direct current; Δt: Speed; φ: Work function; χ: Electron affinity; AC: Alternating current; ECM: Electrochemical metallization; VCM: Valence change mechanism.

Supplementary Information

The online version contains supplementary material available at https://doi.org/10.1186/s11671-022-03699-z.

Additional file 1. Supplementary Materials .

Acknowledgements

Not applicable.

Author contributions

MI contributed to conceptualization, formal analysis, investigation, resources, and writing–original draft. CM was involved in formal analysis and investigation. MK helped in correction of the manuscript and funding acquisition. SK contributed to writing–review and editing, supervision, resources, project administration, and funding acquisition. All authors read and approved the final manuscript.

Funding

This research was supported by National R&D Program through the National Research Foundation of Korea (NRF) funded by Ministry of Science and ICT (2020M3F3A2A01085755) and in part by Basic Science Research Program through the National Research Foundation of Korea (NRF) funded by the Ministry of Education (2018R1A6A1A03023788).

Availability of data and materials

All data generated or analyzed during this study are included in this article and its supplementary information file.

Declarations

Ethics approval and consent to participate

Not applicable.

Consent for publication

Not applicable.

Competing interests

The authors declare they have no competing interests.

Received: 28 February 2022 Accepted: 14 June 2022
Published online: 24 June 2022

References

1. Xia Q, Yang JJ (2019) Memristive crossbar arrays for brain-inspired computing. Nat Mater 18:309–323
2. Zhang Y, Wang Z, Zhu J, et al (2020) Brain-inspired computing with memristors: Challenges in devices, circuits, and systems. Appl Phys Rev 7
3. Sun B, Guo T, Zhou G, et al (2021) Synaptic devices based neuromorphic computing applications in artificial intelligence. Mater Today Phys 18
4. Wong HSP, Salahuddin S (2015) Memory leads the way to better computing. Nat Nanotechnol 10:191–194
5. Wong HSP, Lee HY, Yu S et al (2012) Metal-oxide RRAM. In: Proceedings of the IEEE. Institute of Electrical and Electronics Engineers Inc., pp 1951–1970
6. Lee JS, Lee S, Noh TW (2015) Resistive switching phenomena: a review of statistical physics approaches. Appl Phys Rev 2:031303. https://doi.org/10.1063/1.4929512
7. Lanza M, Wong HSP, Pop E, et al (2019) Recommended methods to study resistive switching devices. Adv Electron Mater 5
8. Shen Z, Zhao C, Qi Y et al (2020) Advances of RRAM devices: Resistive switching mechanisms, materials and bionic synaptic application. Nanomaterials 10:1–31
9. Ismail M, Batool Z, Mahmood K et al (2020) Resistive switching characteristics and mechanism of bilayer HfO2/ZrO2 structure deposited by radio-frequency sputtering for nonvolatile memory. Results Phys. https://doi.org/10.1016/j.rinp.2020.103275

10. Ismail M, Chand U, Mahata C et al (2022) Demonstration of synaptic and resistive switching characteristics in W/TiO2/HfO2/TaN memristor crossbar array for bioinspired neuromorphic computing. J Mater Sci Technol 96:94–102. https://doi.org/10.1016/j.jmst.2021.04.025
11. Ismail M, Mahata C, Kim S (2022) Forming-free Pt/Al2O3/HfO2/HfAlOx/TiN memristor with controllable multilevel resistive switching and neuromorphic characteristics for artificial synapse. J Alloy Compd. https://doi.org/10.1016/j.jallcom.2021.162141
12. Ismail M, Mahata C, Abbas H et al (2021) Bipolar, complementary resistive switching and synaptic properties of sputtering deposited ZnSnO-based devices for electronic synapses. J Alloy Compd. https://doi.org/10.1016/j.jallcom.2020.158416
13. Ismail M, Abbas H, Sokolov A et al (2021) Emulating synaptic plasticity and resistive switching characteristics through amorphous Ta2O5 embedded layer for neuromorphic computing. Ceram Int 47:30764–30776. https://doi.org/10.1016/j.ceramint.2021.07.257
14. Ryu JH, Kim B, Hussain F et al (2021) Bio-inspired synaptic functions from a transparent zinc-tin-oxide-based memristor for neuromorphic engineering. Appl Surf Sci. https://doi.org/10.1016/j.apsusc.2020.148796
15. Ryu JH, Hussain F, Mahata C et al (2020) Filamentary and interface switching of CMOS-compatible Ta2O5 memristor for non-volatile memory and synaptic devices. Appl Surf Sci. https://doi.org/10.1016/j.apsusc.2020.147167
16. Algadi H, Mahata C, Alsuwian T et al (2021) Gradual resistive switching and synaptic properties of ITO/HfAlO/ITO device embedded with Pt nanoparticles. Mater Lett. https://doi.org/10.1016/j.matlet.2021.130011
17. Rana AM, Ismail M, Akber T et al (2019) Transition from unipolar to bipolar, multilevel switching, abrupt and gradual reset phenomena in a TaN/CeO2/Ti: /Pt memory devices. Mater Res Bull 117:41–47. https://doi.org/10.1016/j.materresbull.2019.04.028
18. Kim S, Chen J, Chen YC et al (2019) Neuronal dynamics in HfOx/AlOy-based homeothermic synaptic memristors with low-power and homogeneous resistive switching. Nanoscale 11:237–245. https://doi.org/10.1039/c8nr06694a
19. Ismail M, Rahmani MK, Khan SA et al (2019) Effects of Gibbs free energy difference and oxygen vacancies distribution in a bilayer ZnO/ZrO2 structure for applications to bipolar resistive switching. Appl Surf Sci. https://doi.org/10.1016/j.apsusc.2019.143833
20. Rahmani MK, Ismail M, Mahata C, Kim S (2020) Effect of interlayer on resistive switching properties of SnO2-based memristor for synaptic application. Results Phys. https://doi.org/10.1016/j.rinp.2020.103325
21. Ismail M, Abbas H, Mahata C et al (2022) Optimizing the thickness of Ta2O5 interfacial barrier layer to limit the oxidization of Ta ohmic interface and ZrO2 switching layer for multilevel data storage. J Mater Sci Technol 106:98–107. https://doi.org/10.1016/j.jmst.2021.08.012
22. Liu H, Wei M, Chen Y (2018) Optimization of non-linear conductance modulation based on metal oxide memristors. Nanotechnol Rev 7:443–468
23. Mikhaylov AN, Guseinov DV, Belov AL et al (2021) Stochastic resonance in a metal-oxide memristive device. Chaos Solitons Fractals. https://doi.org/10.1016/j.chaos.2021.110723
24. Meng H, Huang S, Jiang Y (2020) The role of oxygen vacancies on resistive switching properties of oxide materials. AIMS Mater Sci 7:665–683. https://doi.org/10.3934/matersci.2020.5.665
25. Ismail M, Nisa SU, Rana AM et al (2019) Enhancement of resistive switching performance by introducing a thin non-stoichiometric CeO 2–x switching layer in TiO 2 -based resistive random access memory. Appl Phys Lett. https://doi.org/10.1063/1.5066586
26. Ismail M, Abbas H, Choi C, Kim S (2020) Controllable analog resistive switching and synaptic characteristics in ZrO2/ZTO bilayer memristive device for neuromorphic systems. Appl Surf Sci. https://doi.org/10.1016/j.apsusc.2020.147107
27. Ismail M, Abbas H, Choi C, Kim S (2020) Stabilized and RESET-voltage controlled multi-level switching characteristics in ZrO2-based memristors by inserting a-ZTO interface layer. J Alloy Compd. https://doi.org/10.1016/j.jallcom.2020.155256
28. Wang Z, Yin M, Zhang T et al (2016) Engineering incremental resistive switching in TaO: X based memristors for brain-inspired computing. Nanoscale 8:14015–14022. https://doi.org/10.1039/c6nr00476h
29. Xue Q, Wang YC, Wei XH (2019) Synaptic plasticity of room-temperature fabricated amorphous MoO x film based memristor. Appl Surf Sci 479:469–474. https://doi.org/10.1016/j.apsusc.2019.02.092
30. Mahata C, Ismail M, Kim S (2021) Conductance quantization control and neuromorphic properties in Pt-nanoparticle incorporated HfAlOxalloy memristor. Appl Phys Lett. https://doi.org/10.1063/5.0068090
31. Yoon SJ, Ryu JH, Ismail M et al (2019) Compliance current and temperature effects on non-volatile memory switching and volatile switching dynamics in a Cu/SiOx/p++-Si device. Appl Phys Lett. https://doi.org/10.1063/1.5109081
32. Lee M, Lee W, Choi S et al (2017) Brain-inspired photonic neuromorphic devices using photodynamic amorphous oxide semiconductors and their persistent photoconductivity. Adv Mater. https://doi.org/10.1002/adma.201700951
33. Kumar M, Lim J, Park JY et al (2020) Electric-field-induced healing of inanimate topographies: multistate resistive switching and nano-sized artificial synapse functionality. Appl Surf Sci. https://doi.org/10.1016/j.apsusc.2020.147190
34. Kim SG, Han JS, Kim H, et al (2018) Recent advances in memristive materials for artificial synapses. Adv Mater Technol 3
35. Serb A, Corna A, George R et al (2020) Memristive synapses connect brain and silicon spiking neurons. Sci Rep. https://doi.org/10.1038/s41598-020-58831-9
36. Jo SH, Chang T, Ebong I et al (2010) Nanoscale memristor device as synapse in neuromorphic systems. Nano Lett 10:1297–1301. https://doi.org/10.1021/nl904092h
37. Ohno T, Hasegawa T, Tsuruoka T et al (2011) Short-term plasticity and long-term potentiation mimicked in single inorganic synapses. Nat Mater 10:591–595. https://doi.org/10.1038/nmat3054
38. Kim S, Du C, Sheridan P et al (2015) Experimental demonstration of a second-order memristor and its ability to biorealistically implement synaptic plasticity. Nano Lett 15:2203–2211. https://doi.org/10.1021/acs.nanolett.5b00697
39. Rana AM, Akbar T, Ismail M et al (2017) Endurance and cycle-to-cycle uniformity improvement in tri-layered CeO2 /Ti/CeO2 resistive switching devices by changing top electrode material. Sci Rep. https://doi.org/10.1038/srep39539
40. Ismail M, Ahmed E, Rana AM et al (2016) Improved endurance and resistive switching stability in ceria thin films due to charge transfer ability of Al dopant. ACS Appl Mater Interfaces 8:6127–6136. https://doi.org/10.1021/acsami.5b11682
41. Zhou F, Zhou Z, Chen J et al (2019) Optoelectronic resistive random access memory for neuromorphic vision sensors. Nat Nanotechnol 14:776–782. https://doi.org/10.1038/s41565-019-0501-3
42. Zhu X, Su W, Liu Y et al (2012) Observation of conductance quantization in oxide-based resistive switching memory. Adv Mater 24:3941–3946. https://doi.org/10.1002/adma.201201506
43. Sharath SU, Vogel S, Molina-Luna L et al (2017) Control of switching modes and conductance quantization in oxygen engineered HfOx based memristive devices. Adv Func Mater. https://doi.org/10.1002/adfm.201700432
44. Park J, Lee S, Lee K, Kim S (2021) Conductance quantization behavior in pt/sin/tan rram device for multilevel cell. Metals (Basel). https://doi.org/10.3390/met11121918
45. Zhang Y, Wu Z, Liu S et al (2021) A quantized convolutional neural network implemented with memristor for image denoising and recognition. Front Neurosci. https://doi.org/10.3389/fnins.2021.717222
46. Yeon H, Lin P, Choi C et al (2020) Alloying conducting channels for reliable neuromorphic computing. Nat Nanotechnol 15:574–579. https://doi.org/10.1038/s41565-020-0694-5
47. Xie Z, Gao S, Ye X et al (2020) Magnetism modulation and conductance quantization in a gadolinium oxide memristor. Phys Chem Chem Phys 22:26322–26329. https://doi.org/10.1039/d0cp03767b
48. Gao S, Chen C, Zhai Z et al (2014) Resistive switching and conductance quantization in Ag/SiO 2/indium tin oxide resistive memories. Appl Phys Lett. https://doi.org/10.1063/1.4893277
49. Chen C, Gao S, Zeng F et al (2013) Conductance quantization in oxygen-anion-migration-based resistive switching memory devices. Appl Phys Lett. https://doi.org/10.1063/1.4816747
50. Zhang W, Kong JZ, Cao ZY et al (2017) Bipolar resistive switching characteristics of HfO2/TiO2/HfO2 trilayer-structure RRAM devices on Pt and

TiN-coated substrates fabricated by atomic layer deposition. Nanoscale Res Lett. https://doi.org/10.1186/s11671-017-2164-z
51. Wang LG, Qian X, Cao YQ et al (2015) Excellent resistive switching properties of atomic layer-deposited Al2O3/HfO2/Al2O3 trilayer structures for non-volatile memory applications. Nanoscale Res Lett. https://doi.org/10.1186/s11671-015-0846-y
52. Ismail M, Mahata C, Kim S (2022) Tailoring the electrical homogeneity, large memory window, and multilevel switching properties of HfO2-based memory through interface engineering. Appl Surf Sci 581:152427. https://doi.org/10.1016/j.apsusc.2022.152427
53. di Huang X, Li Y, Li HY et al (2020) Forming-free, fast, uniform, and high endurance resistive switching from cryogenic to high temperatures in W/AlOx/Al2O3/Pt bilayer memristor. IEEE Electron Device Lett 41:549–552. https://doi.org/10.1109/LED.2020.2977397
54. Morikawa T, Saeki S, Suzuki T et al (2010) Dual functional modification by N doping of Ta2 O5: P-type conduction in visible-light-activated N-doped Ta2 O 5. Appl Phys Lett. https://doi.org/10.1063/1.3386532
55. Syu YE, Zhang R, Chang TC et al (2013) Endurance improvement technology with nitrogen implanted in the interface of WSiOx resistance switching device. IEEE Electron Device Lett 34:864–866. https://doi.org/10.1109/LED.2013.2260125
56. Marchack N, Innocent-Dolor J, Hopstaken M, Engelmann S (2020) Control of surface oxide formation in plasma-enhanced quasiatomic layer etching of tantalum nitride. J Vac Sci Technol, A 38:022609. https://doi.org/10.1116/1.5140457
57. Yang J, Cho H, Ryu H et al (2021) Tunable synaptic characteristics of a Ti/TiO2/Si memory device for reservoir computing. ACS Appl Mater Interfaces 13:33244–33252. https://doi.org/10.1021/acsami.1c06618
58. Lin J, Wang S, Liu H (2021) Multi-level switching of al-doped HfO2 RRAM with a single voltage amplitude set pulse. Electronics (Switzerland) 10:1–10. https://doi.org/10.3390/electronics10060731
59. Kim W, Menzel S, Wouters DJ et al (2016) Impact of oxygen exchange reaction at the ohmic interface in Ta2O5-based ReRAM devices. Nanoscale 8:17774–17781. https://doi.org/10.1039/c6nr03810g
60. Abbaspour E, Menzel S, Jungemann C (2020) Studying the switching variability in redox-based resistive switching devices. J Comput Electron 19:1426–1432. https://doi.org/10.1007/s10825-020-01537-y
61. Krans J, Muller CJ, Yanson IK, et al One-atom point contacts
62. Li L, Chen Y, Cai C et al (2021) Single crystal halide perovskite nonlinear resistive memory with ultrahigh switching ratio. Small. https://doi.org/10.1002/smll.202103881
63. Yi W, Savel'Ev SE, Medeiros-Ribeiro G et al (2016) Quantized conductance coincides with state instability and excess noise in tantalum oxide memristors. Nat Commun. https://doi.org/10.1038/ncomms11142
64. Sahu VK, Misra P, Das AK, et al (2017) Quantized conductance in Ta2O5 based resistive random access memory devices. In: AIP Conference Proceedings. American Institute of Physics Inc.
65. Zhao J, Zhou Z, Zhang Y et al (2019) An electronic synapse memristor device with conductance linearity using quantized conduction for neuroinspired computing. J Mater Chem C 7:1298–1306. https://doi.org/10.1039/c8tc04395g
66. Bersuker G, Gilmer DC, Veksler D (2019) Metal-oxide resistive random access memory (RRAM) technology: material and operation details and ramifications. In: Advances in non-volatile memory and storage technology. Elsevier, New York, pp 35–102
67. Arruda TM, Kumar A, Kalinin SV, Jesse S (2011) Mapping irreversible electrochemical processes on the nanoscale: Ionic phenomena in li ion conductive glass ceramics. Nano Lett 11:4161–4167. https://doi.org/10.1021/nl202039v
68. Mohanty SK, Reddy PK, Prasad OK et al (2021) Interface engineering for 3-bit per cell multilevel resistive switching in AlN based memristor. IEEE Electron Device Lett 42:1770–1773. https://doi.org/10.1109/LED.2021.3125151
69. Wang S, Dang B, Sun J et al (2020) Physically transient W/ZnO/MgO/W schottky diode for rectifying and artificial synapse. IEEE Electron Device Lett 41:844–847. https://doi.org/10.1109/LED.2020.2986837
70. Lee J, Ryu JH, Kim B et al (2020) Synaptic characteristics of amorphous boron nitride-based memristors on a highly doped silicon substrate for neuromorphic engineering. ACS Appl Mater Interfaces 12:33908–33916. https://doi.org/10.1021/acsami.0c07867
71. Voglis G, Tavernarakis N (2006) The role of synaptic ion channels in synaptic plasticity. EMBO Rep 7:1104–1110
72. Hu SG, Liu Y, Chen TP et al (2013) Emulating the Ebbinghaus forgetting curve of the human brain with a NiO-based memristor. Appl Phys Lett. https://doi.org/10.1063/1.4822124
73. Abbott LF, Regehr WG (2004) Synaptic computation. Nature 431:796–803. https://doi.org/10.1038/nature03010
74. Dean JA (1990) Lange's handbook of chemistry. Mater Manuf Processes 5:687–688. https://doi.org/10.1080/10426919008953291
75. Hong SM, Kim HD, An HM, Kim TG (2013) Effect of work function difference between top and bottom electrodes on the resistive switching properties of SiN films. IEEE Electron Device Lett 34:1181–1183. https://doi.org/10.1109/LED.2013.2272631
76. Ismail M, Talib I, Rana AM et al (2018) Effect of bilayer CeO2−x/ZnO and ZnO/CeO2−x heterostructures and electroforming polarity on switching properties of non-volatile memory. Nanoscale Res Lett. https://doi.org/10.1186/s11671-018-2738-4
77. Jabeen S, Ismail M, Rana AM, Ahmed E (2017) Impact of work function on the resistive switching characteristics of M/ZnO/CeO2/Pt devices. Materials Research Express. https://doi.org/10.1088/2053-1591/aa6dec
78. Hsu CC, Sun JK, Tsao CC, Chuang PY (2017) Effects of Gibbs free energy of interfacial metal oxide on resistive switching characteristics of solution-processed HfOx films. Physica B 519:21–25. https://doi.org/10.1016/j.physb.2017.05.040
79. Li Q, Qiu L, Wei X et al (2016) Point contact resistive switching memory based on self-formed interface of Al/ITO. Sci Rep. https://doi.org/10.1038/srep29347
80. Xu X, Rajendran B, Anantram MP (2020) Kinetic Monte Carlo simulation of interface-controlled hafnia-based resistive memory. IEEE Trans Electron Devices 67:118–124. https://doi.org/10.1109/TED.2019.2953917
81. Zhou P, Yin M, Wan HJ et al (2009) Role of TaON interface for CuxO resistive switching memory based on a combined model. Appl Phys Lett. https://doi.org/10.1063/1.3078824
82. Valov I (2017) Interfacial interactions and their impact on redox-based resistive switching memories (ReRAMs). Semiconduct Sci Technol 32
83. Ryu JH, Kim S (2020) Artificial synaptic characteristics of TiO2/HfO2 memristor with self-rectifying switching for brain-inspired computing. Chaos Solitons Fractals. https://doi.org/10.1016/j.chaos.2020.110236
84. Akbari M, Kim MK, Kim D, Lee JS (2017) Reproducible and reliable resistive switching behaviors of AlOX/HfOX bilayer structures with Al electrode by atomic layer deposition. RSC Adv 7:16704–16708. https://doi.org/10.1039/c6ra26872b
85. Mahata C, Kang M, Kim S (2020) Multi-level analog resistive switching characteristics in tri-layer hfo2/al2o3/hfo2 based memristor on ito electrode. Nanomaterials 10:1–12. https://doi.org/10.3390/nano10102069

Publisher's Note